Technische Universität München
Fakultät für Physik

Abschlussarbeit im Bachelorstudiengang Physik

Leakage Studies for the analysis of Diffractive Dissociation into the $\pi^-\pi^-\pi^+$ final state

Stefan Lietzau

September 30, 2013

Erstgutachter (Themensteller): Prof. S. Paul
Zweitgutachter: Prof. F. Eisenhauer

Contents

1 Motivation

In the early days of high–energy physics a system was needed to classifify all the new particles. The *constituent quark model* was the first model able to explain the variety of observed hadrons. The model describes mesons as $(q\bar{q})$ and baryons as (qqq) not taking attractive potential between the two fermions into account.

Some years later quantum chromodynamics(**QCD**) was developed and accepted as theory for the strong interaction. Unlike the coupling constant for the electromagnetic interaction, the coupling constant for the strong force, α_s, is not constant but increases towards low energies. As a result it is not possible to perform perturbation calculation in the low energy region, because the series does not converge for high orders. One method to overcome this problem is to use *Lattice QCD* to calculate a solution using Monte-Carlo techniques. Since this requires a huge amount of CPU power and time, which was not available 40 years ago, the constituent quark model is often used for calculations.

QCD allows states which are combinations of quarks and gluons, so called *hybrids*, and glueballs. These states cannot be explained by the quark model. If the QCD would be the right theory to describe low energy interaction one would expect to find such gluonic states. Most of the hybrid states have quantum numbers allowed in the

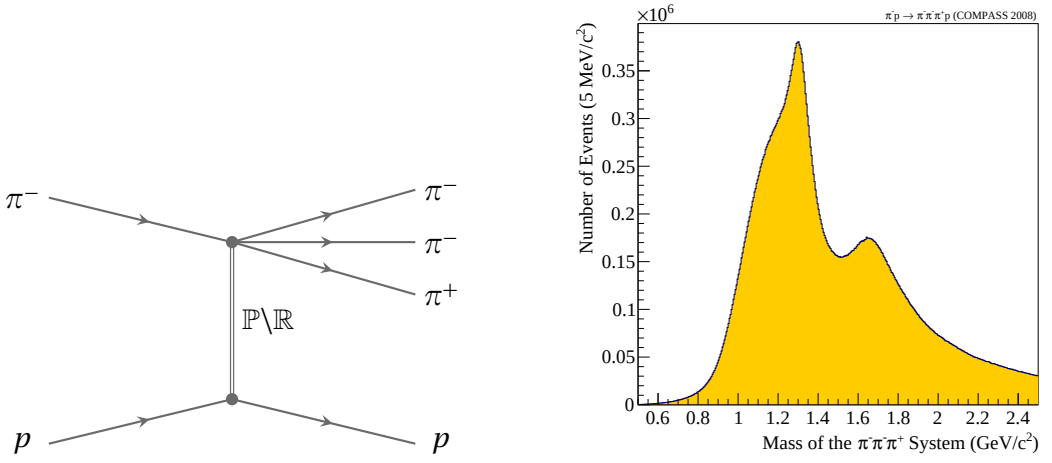

Figure 1.1: The reaction happening in COMPASS is pictured on the left. On the right the observed invariant mass spectrum of the real data is shown.

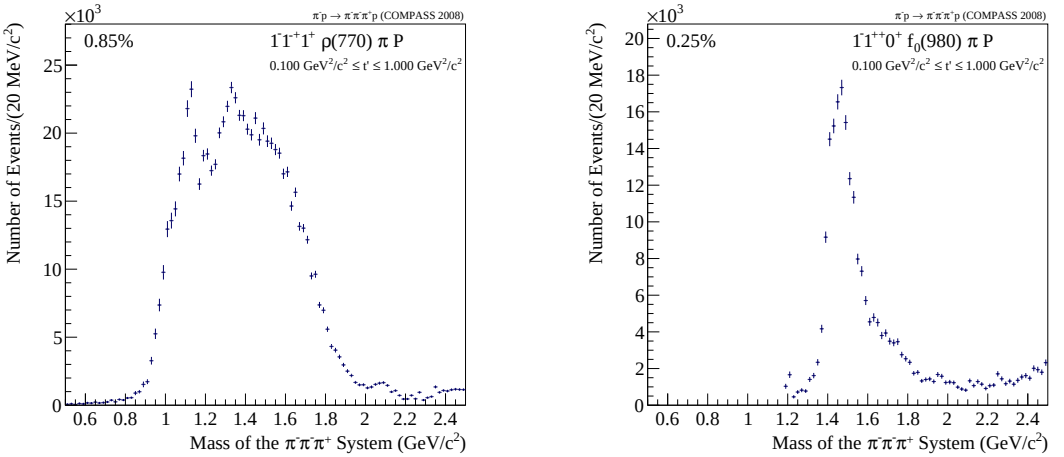

Figure 1.2: Intensities of the two important partial waves as extracted by the PWA.

constituent quark model so it is difficult to tell them apart from pure $q\bar{q}$ states. The only way to exclude quark–model states is to look for so called *spin exotics*, states with quantum numbers forbidden in the quark model. Finding them would confirm the QCD as theory for the strong interaction in the low energy region. There has been experimental evidence for the existence of spin exotics, which are states with J^{PC} quantum numbers not possible for $(q\bar{q})$. One possible candidate is the $\pi_1(1600)$ with $J^{PC} = 1^{-+}$ which was found in several experiments, including the pilot run of COMPASS in 2004[1].

One key aim of the COMPASS experiment is to analyze the light–meson spectrum and find hybrids. To achieve this, in the year 2008, the largest dataset for the reaction $\pi^- + p \to \pi^-\pi^-\pi^+ + p$ was taken. In the analysis of the 2008 data[4], beside the expected intensity for the major resonances($a_1(1260)$, $a_2(1320)$ and $\pi_2(1670)$), the intensity shown in figure 1.2(left) was observed for the spin-exotic candidate.

For another partial wave intensity was observed as shown in figure 1.2 on the right. Interesting about this is the fact, that there are no known resonances for this set of quantum numbers in the $1.4\,\mathrm{GeV}/c^2$ mass region, where the data exhibits a pronounced peak and no theory predictes observing intensity in this region. So this state is something completely unknown.

The goal of this bachelor thesis is a systematic study of the partial–wave analysis(**PWA**)[4] in order to determine whether artifacts do affect the output. To accomplish this a weighted monte carlo study will be done to compare the simulated output for different scenarios.

2 The COMPASS Experiment

The experiment is located at CERN and connected to the **SPS** (**S**uper **P**roton **S**ynchrotron). One of the advantages of the **COMPASS** Spectrometer (**Co**mmon **M**uon and **P**roton **A**pparatus for **S**tructure and **S**pectroscopy)[3] is the fact that it can run with a muon or a hadron beam. It is a fixed–target experiment with a two-stage magnet spectrometer.

2.1 The Beamline

COMPASS is connected to the SPS which delivers a 400 GeV/c primary proton beam. In the collision with a Beryllium target the negative secondary hadron beam is created. At the COMPASS target this beam consists of 96.8% π^-, 2.8% K^- and 0.8% $\bar{p}$. At arrival the beam has a momentum of 190 GeV/c. The incoming particles are identified using cherenkov detectors(CEDARS).

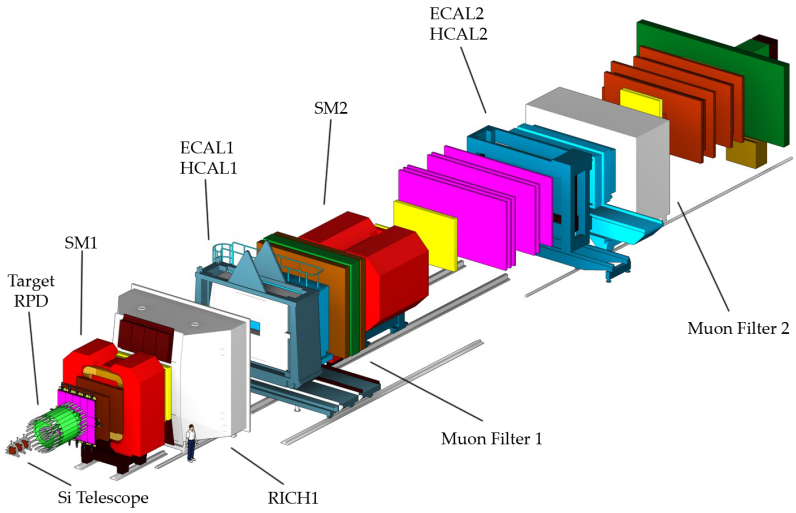

Figure 2.1: The COMPASS setup for the run in 2008.

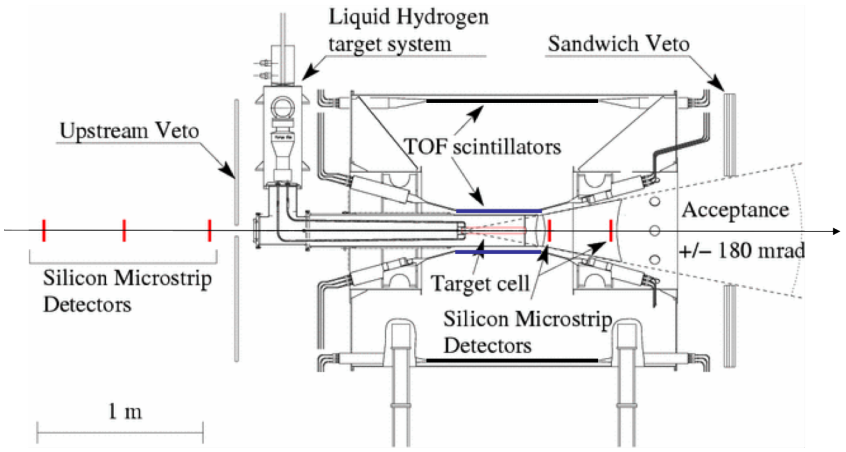

Figure 2.2: Overview of the target region showing beam, the RPD which detects the recoil proton and the Si detectors for vertex reconstruction

2.2 Target Area

A recoil proton detector (**RPD**) is used, since the exclusion measurement is essential for this experiment. As it can be seen in figure 2.2 the RPD consists of two cylinders around the target. Upstream of the target a system of silicon detectors, the beam telescope, measures the incoming beam particles. Downstream a pair of silicon detectors allows precise vertex reconstruction. Since COMPASS is a fixed–target experiment, high resolution detectors, such as silicon detectors, are needed close to the beam axis. Liquid hydrogen serves as a target.

2.3 Charged Particle Tracking

A fixed–target experiment has high intensity near the beam which then decreases rapidly towards larger angles. Because of this, staggered tracking is used. This means there are small high–resolution detectors, as for example silicon detectors with an area of 10 x 16mm^2, with high accuracy and rate in the center of the beam and large detectors, like drift champers with an area of 3 x 4m^2, which cover the outer regions.

For neutral particle detection two calorimeters are used. Since the final state particles of the channel analyzed here are charged the calorimeters are not described in detail.

3 Background for the analysis

3.1 Partial–wave analysis method

To analyze the reaction shown in figure 1.1 one assumes the production of an intermediate excited state X^- and its subsequent decay to an isobar ξ and a single π^-. Shown in figure 3.1 is the reaction in the isobar model. The quantum numbers $J^{PC}M^{\epsilon}$ represent the X^- which decays at vertex 1 to the isobar. The ξ decays at vertex 2 further to a $\pi^-$and π^+. With this model one can calculate the production and decay of the X^- independently. This leads to the following formula for the kinematic distribution of the final–state particles:

$$I\left(m_X, t, \tau\right) = \left| \sum_i \tilde{T}_i(m_X, t) \sum_j \tilde{\Psi}_{i,j}(m_X, \tau) \right|^2 \tag{3.1}$$

The I describes the observed intensity for a specific mass of the excited state, m_X, for the squared four–momentum transfer $t^{'}$ and the set of phase–space variables τ. This intensity is the product of all production amplitudes $\tilde{T}_i$ and decay amplitudes $\tilde{\Psi}_{i,j}$. In this summation i stands for all possible quantum numbers of the X^- whereas j includes all possible decay channels.

I is a function depending on seven variables. To reduce model bias the $m_{3\pi}$ and $t^{'}$ will not be modeled but the analysis will be performed in narrow bins, where I does not depend on $m_{3\pi}$ and $t^{'}$ anymore This increases the number of parameters but reduces model dependence. The mass range from $0.5\,\mathrm{GeV}/c^2$ to $2.5\,\mathrm{GeV}/c^2$ is

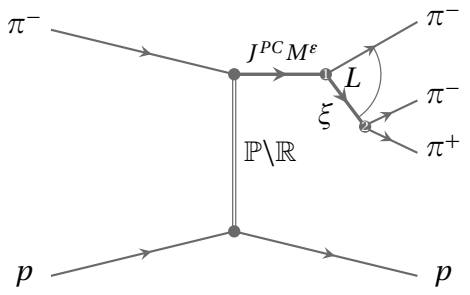

Figure 3.1: The production and decay using the Isobar model

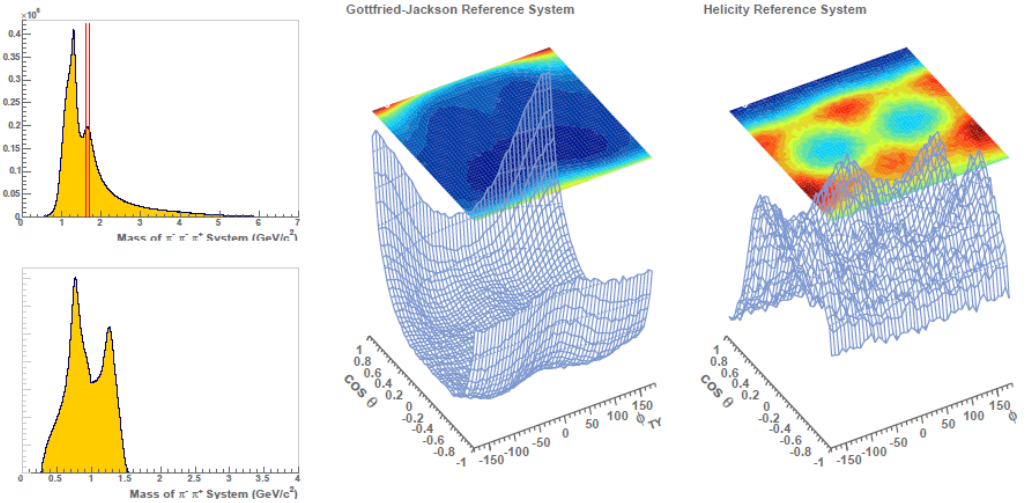

Figure 3.2: Distribution of the phase space variables τ in the Gottfried-Jackson frame and in the helecity frame calculated for a $m_{3\pi}$ bin around $1.670\,\mathrm{GeV}/c^2$.

split into 100 bins of $20\,\mathrm{MeV}/c^2$ width each. The momentum transfer t' is split into 11 bins which will be detailed further in chapter 4. The τ is a set of 5 phase space variables describing the angles at vertex 1 and 2 in specific coordinates. At vertex 1 the Gottfried-Jackson frame and and vertex 2 the Helecity frame is used.[4] A sample distribution is shown in figure 3.2 for a small mass range around $1.670\,\mathrm{GeV}/c^2$.

In the next step the unknown couplings appearing at vertex 1 and 2 are moved from the decay amplitude to the production amplitude creating the transition amplitude $T_{i,j}$ which now depends on j, too. i and j are merged to the partial–wave

$$\alpha = J^{PC}\, M^{\epsilon}\, \xi\, \pi^{-}\, L. \tag{3.2}$$

The term $J^{PC}M^{\epsilon}$ describes the quantum numbers of the excited X^{-} as seen in 3.1. The reflectivity ϵ is needed for parity conservation. The decay channel is classified as $\xi\,\pi^{-}\,L$ with the isobar ξ and the orbital momentum L between the isobar and bachelor pion at vertex 1. This makes α a unique classification for a partial–wave. With this changes equation 3.1 reads as:

$$I\left(\tau\right) = \left|\sum_{\alpha}\, T_{\alpha}\, \Psi_{\alpha}\left(\tau\right)\right|^{2} \tag{3.3}$$

In this equation the intensity $I\left(\tau\right)$ is derived from the data, the decay amplitudes $\Psi_{\alpha}\left(\tau\right)$ can be calculated and the transition amplitudes T_{α} are unknown.

The square of the absolute value in equation (3.3) can be expanded to

$$I(\tau) = \sum_{i,j} T_i \, T_j^* \; \Psi_i \, \Psi_j^*. \tag{3.4}$$

This function is a model for the five–dimensional distribution of the final–state pions for one kinematic bin (m_X, t'). With (3.4) one can employ an unbinned extended maximum likelihood fit to calculate $T_i \, T_j^*$ taking into account the detector acceptance. The two terms for the transition amplitude can be combined to create a spin–density matrix $\rho_{i,j} = T_i \, T_j^*$. This matrix describes the production of each intermediate state and the phase motion between different states. A sample submatrix is shown in figure 3.3.

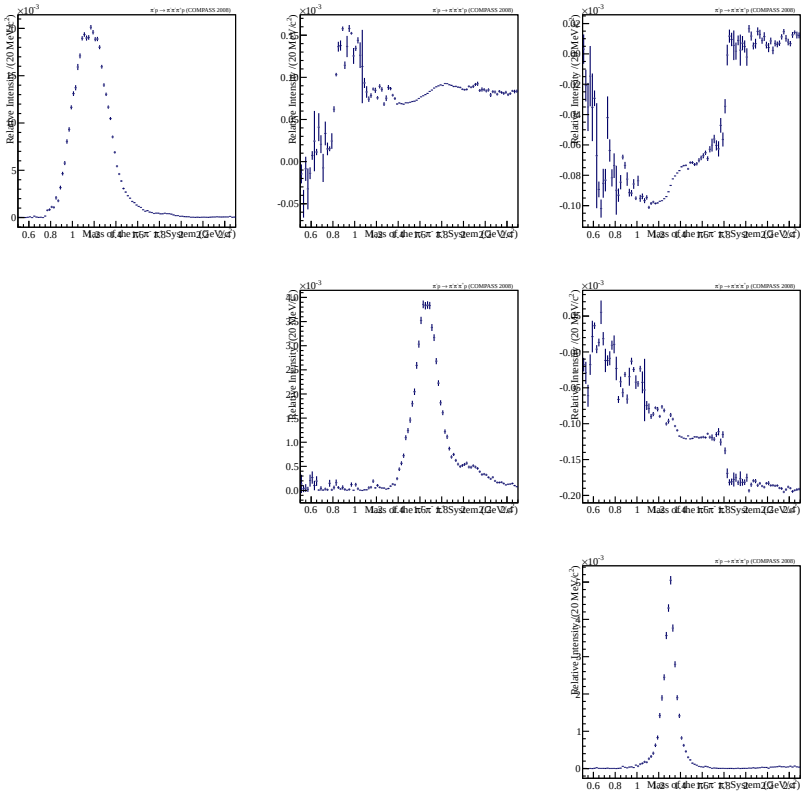

Figure 3.3: Matrix showing the intensities for the three major waves on the diagonal and the relative phase between the waves on the off–diagonal parts. The data used was the Monte-Carlo sample including all partial–waves for t'-bin 2 (see table A.1 for explanation of the tbins).

3.2 Motivation for Leakage Study

In theory partial–waves with different $J^{PC}M^{\epsilon}$ are orthogonal. Because of resolution effects the orthogonality of the amplitudes in the data gets disturbed. This could cause cross-talk between partial–waves resulting in intensity of one wave flowing to another. Since the fit program is taking acceptance effects into account, it is possible to do a consistency check for the acceptance correction. It is also possible that some artifacts occur during the reconstruction process. All this can result in a partial–wave getting more intensity than it normally would which is called *leakage*. Since these effects can happen in any partial–wave analysis it is common practice to perform a leakage study to verify the results.

It is important to note that finding the source of the leakage is way more complicated than measuring its contribution. The idea of doing a leakage study is to generate a Monte-Carlo data set with a known partial–wave composition, simulate it and compare the simulated output with the known input. There are two common ways of doing this. The first being to create events for **only one** partial–wave and the second one being to create events for **all but one** partial–wave. The result is compared to a reference with all partial waves activated.

3.3 Simulation Chain

The leakage analysis is done in five steps. Each one is detailed further below. First events are created according to a known partial–wave distribution. Then the traversal of particles through the detector is simulated. In the next step this information is used to reconstruct particle tracks using the same approach as for real data. The reconstructed events get filtered. At last the partial–wave analysis is applied to this filtered data.

1. **Event Generation** To generate Events corresponding to a specific set of partial–waves one needs the production amplitudes which are obtained by a prior partial–wave analysis of real data. The generation is done for each combination of bins in t' and $m_{3\pi}$. Events are created according to the fit function (3.4) using sample–and–reject methods.

2. **Monte Carlo Simulation**

   For the simulation of the processes inside the spectrometer a modified version of GEANT3, COMGEANT[1] is used. This software uses Monte-Carlo techniques to calculate all known physical processes happening inside the detector materials. The output of COMGEANT is an example to what could have happened during

[1] http://wwwcompass.cern.ch/twiki/bin/view/DataReconstruction/MonteCarlo#COMGEANT

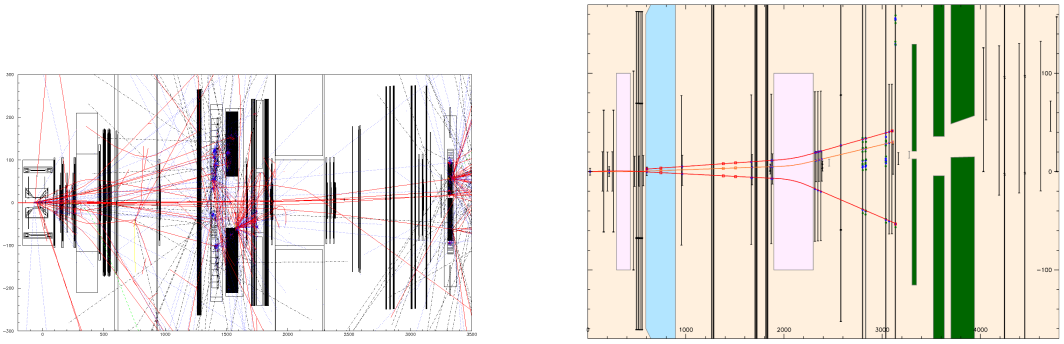

Figure 3.4: Output of ComGeant (left) after simulating all physical processes. Reconstruction of the ComGeant output done by Coral(right). In the Coral Output the two staged detection is plainly visible.

a real run. An example of the simulated data produced by ComGeant is shown in figure 3.4.

3. **Reconstruction**

   The output of ComGeant needs to be filtered and the tracks of the particles need to be reconstructed from the detector information. This is done by clustering the measured hits and then connecting the clusters to create tracks. The program used is Coral[2], which is also used for real-data analysis. The output is saved as a mdst(Mini Data Summary Table) file and includes the information shown in figure 3.4 Which contain the data in the same way as for real data with the addition of the Monte Carlo truth variables, the data which was put into the analysis chain. This is useful to calculate the acceptance and efficiency of the detectors.

4. **Event Selection**

   After the simulation and reconstruction the event selection is performed on the reconstructed events. The same selection criteria as for real data are used. The selection is done by the PHAST[2] program using an event selection algorithm[4]. During this process $\approx$ 75% of the events are discarded. An list of the performed cuts can be found in [4].

5. **Performing the Partial–Wave Analysis**

   The transition amplitude is calculated using by fitting the intensity contribution with a know decay composition. In the last step for each mass and t'-bin

[2] http://wwwcompass.cern.ch/twiki/bin/view/DataReconstruction/CoralSoftware

all events are used to create the intensity distribution for the phase space variables. This distribution together with the decay amplitudes is used to create the transition amplitudes from which the spin–density matrix is calculated.

The spin density matrix provides information of the intensity for each partial–wave and the phase motion between the waves. Doing this for each kinematic bin one can create a distribution of the three–pion mass $m_{3\pi}$ for each partial–wave showing the amount of events populating this state.

4 Leakage Analysis

For the analysis the events were binned as shown in figure 4.1. Each rectangle represents one kinematic bin in t' and $m_{3\pi}$. On the left the t'-distribution is shown in logarithmic scale. The intensity decreases rapidly with higher t'. For the analysis the t'-bins were chosen to contain an approximately equal amount of events, resulting in the bin ranges shown in table A.1. These are the bins used to fragment the whole range of $0.1\,\mathrm{GeV}^2/c^2 - 1.0\,\mathrm{GeV}^2/c^2$. To investigate the behavior for high and low momentum transfer and reduce required computing power the analysis was limited to t'–bin 2 and 9.

As mentioned in the motivation the analysis was performed for the two interesting partial waves. Additionally the three major waves which produce the structure seen in figure 1.1 were analyzed. Together with a reference containing all partial waves a total of 12 data sets were generated. For the major waves the method of producing only one specific wave was used whereas for $1^{-+}\,1^{+}\,\rho(770)\,\pi\,P$and $1^{++}\,0^{+}\,f_0(980)\,\pi\,P$, the other method to generate all but one partial wave was used.

Table 4.1 shows the events generated for each partial wave and the total intensity

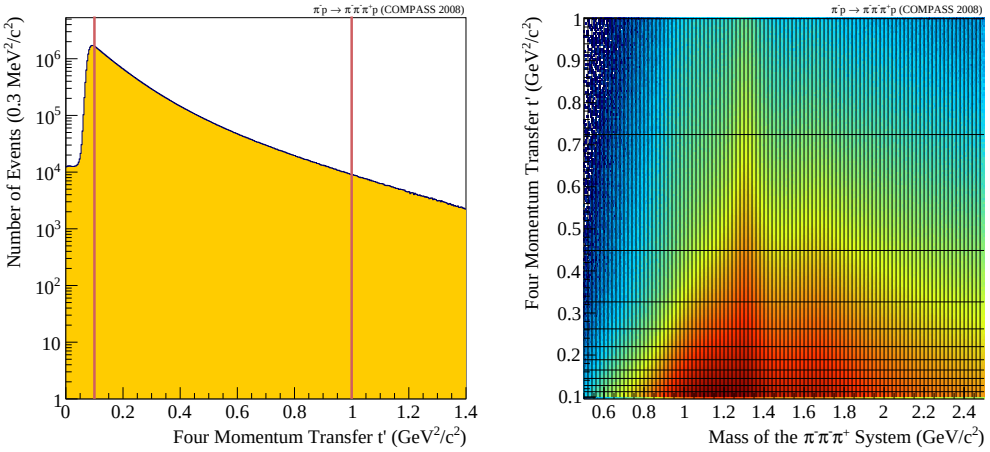

Figure 4.1: On the left the overall distribution of events depending on the t' is shown in logarithmic scale. The right plot shows die distribution of events in a two dimensional histogram where the y axis reflects t' and the x axis $m_{3\pi}$. The z axis shows the observed intensity.

Partial Wave	generated Events		Intensity in real data	
	t'–bin 2	t'–bin 9	t'–bin 2	t'–bin 9
Full waveset	13 949 059	7 958 790	-	-
$1^{++}\,0^{+}\,\rho(770)\,\pi\,S$	7 344 114	8 252 254	0.3939	0.2338
$2^{++}\,1^{+}\,\rho(770)\,\pi\,D$	8 586 682	8 219 762	0.0388	0.1389
$2^{-+}\,0^{+}\,f_2(1270)\,\pi\,S$	7 776 352	7 758 992	0.0661	0.0706
$1^{-+}\,1^{+}\,\rho(770)\,\pi\,P$	13 402 896	7 637 926	0.0074	0.0097
$1^{++}\,0^{+}\,f_0(980)\,\pi\,P$	11 211 178	6 311 366	0.0024	0.0028

Table 4.1: Overview of the amount of generated events for each partial wave.

of that wave. The parameters for the generation were chosen as to leave at least 5×10^6 events successfully reconstructed by CORAL.

4.1 Comparison of Monte Carlo data with real data

The first thing to look into when working with simulated data is to validate the the data. In this case this can be done by comparing it to the real data. In figure 4.2 the incoherent sum over all partial waves is show for real data and simulated data. The shape looks the same but in detail there are some minor differences. The two peaks seen at $1.2\,\mathrm{GeV}/c^2$ and $1.7\,\mathrm{GeV}/c^2$ in the plot for the t'-bin 2 have different heights. The first peak is overestimated by the monte carlo whereas the second peak is underestimated. For masses above $2.2\,\mathrm{GeV}/c^2$ the monte carlo overestimates again.

To understand the difference seen in figure 4.2 one can look at the distribution of the partial waves inside the data. The distribution for the t'–bin 2 is shown in figure 4.3. There are some minor differences. $1^{++}\,0^{+}\,\rho(770)\,\pi\,S$ gets overestimated while $2^{++}\,1^{+}\,\rho(770)\,\pi\,D$ gets underestimated. They have all high intensities what explains the derivations of the two peaks in figure 4.3.Looking at the $m_{3\pi}$ spectra of the three major partial waves(see section 4.2) one can see that these waves have high intensity in the regions where the differences in the incoherent sum are visible.

There are no huge differences between the two t'–bins so only plots for t'–bin 2 will be shown in this chapter, the corresponding plots for t'–bin 9 can be found in the appendix.

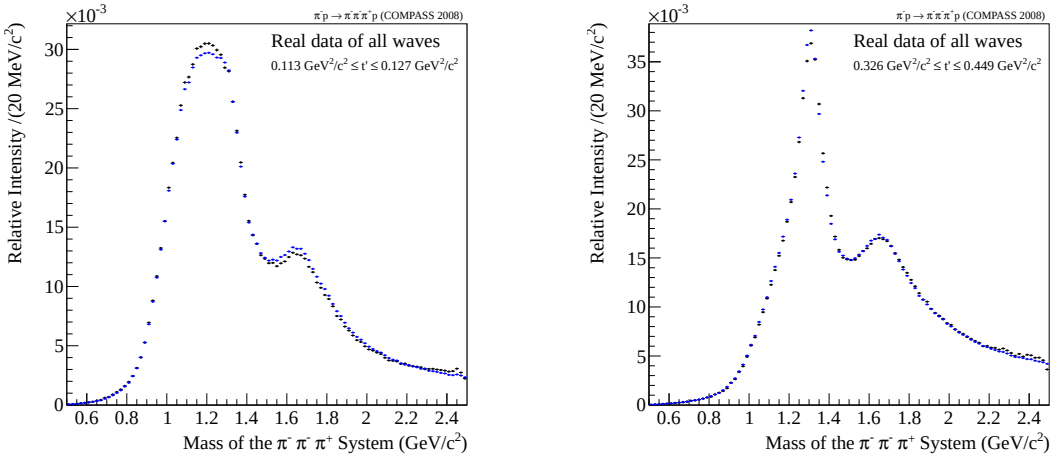

Figure 4.2: The normalized distribution of the $m_{3\pi}$ for the real data (in blue) and the simulation with all waves activated (in black). Left is t'–bin 2 and right t'–bin 9

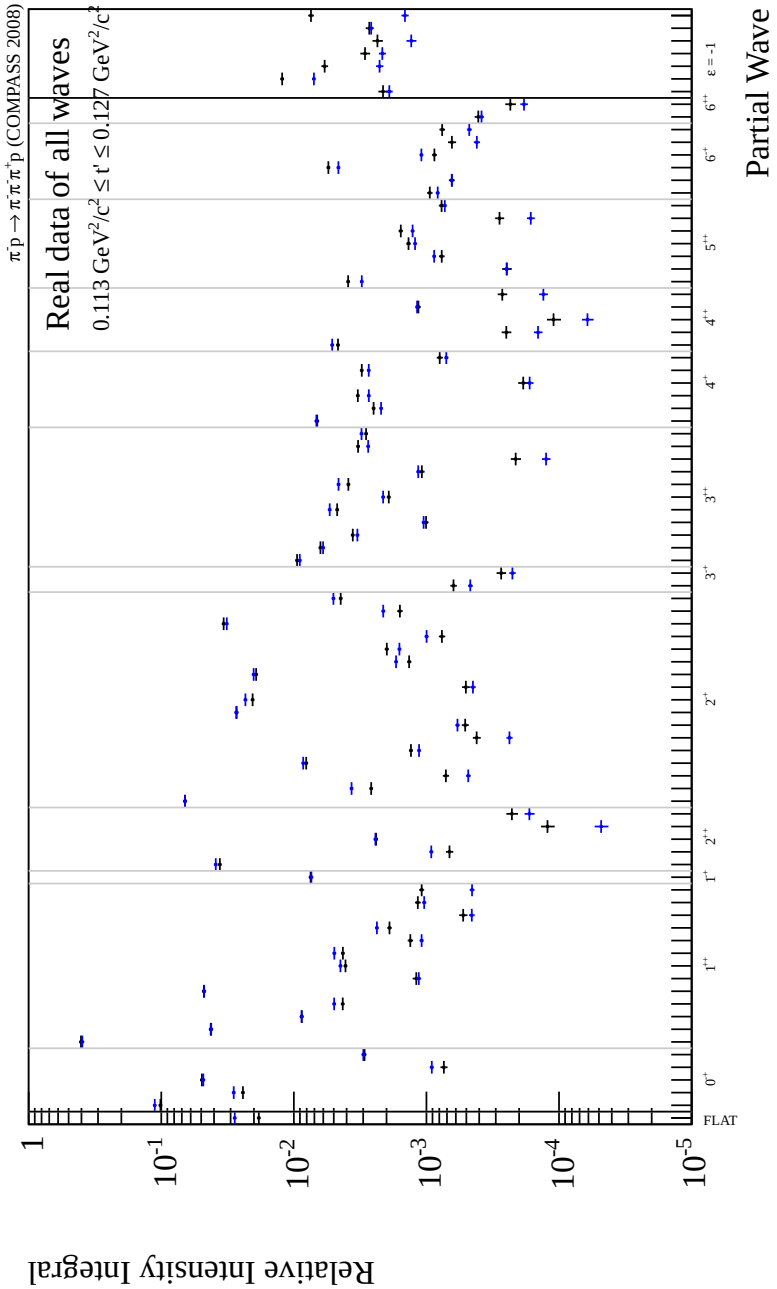

Figure 4.3: Comparison of real data (in blue) and simulated data (in black). Shown is the intensity integral for each partial wave comparing real data with Monte Carlo output

4.2 Leakage from the three major waves

This set of studies was done to analyze the leakage coming from the three major waves. Since these waves have the highest intensities and leakage is known to scale with the intensity it is obvious to start looking for leakage with this waves. On top of that leakage created by a high intensity wave into a low intensity wave has a huge impact on the $m_{3\pi}$ distribution of that partial wave and could cause virtual peaks. The summary of the outgoing leakage of the three major waves is shown in table 4.2. Taking the intensity and leakage of one wave, one can calculate the total leakage produced by this wave. Summing this up for the three main waves yields less then 5% of the total intensity is affected by leakage.

As seen in figures 4.4, 4.5 and 4.6 there is only the wave marked by red lines with high intensity. Shown in figure 4.7 is the $m_{3\pi}$ distribution of the three major waves. There is almost no difference between simulation and real data. The only derivation is the overestimation of the $1^{++}\,0^{+}\,\rho(770)\,\pi\,S$ in the middle of the peak.

Partial wave	t'–bin 2	t'–bin 9
$1^{++}\,0^{+}\,\rho(770)\,\pi\,S$	0.0423	0.0294
$2^{++}\,1^{+}\,\rho(770)\,\pi\,D$	0.0276	0.0154
$2^{-+}\,0^{+}\,f_2(1270)\,\pi\,S$	0.0140	0.0070

Table 4.2: Leakage from the major waves. The amount of leakage is the intensity missing to 100%.

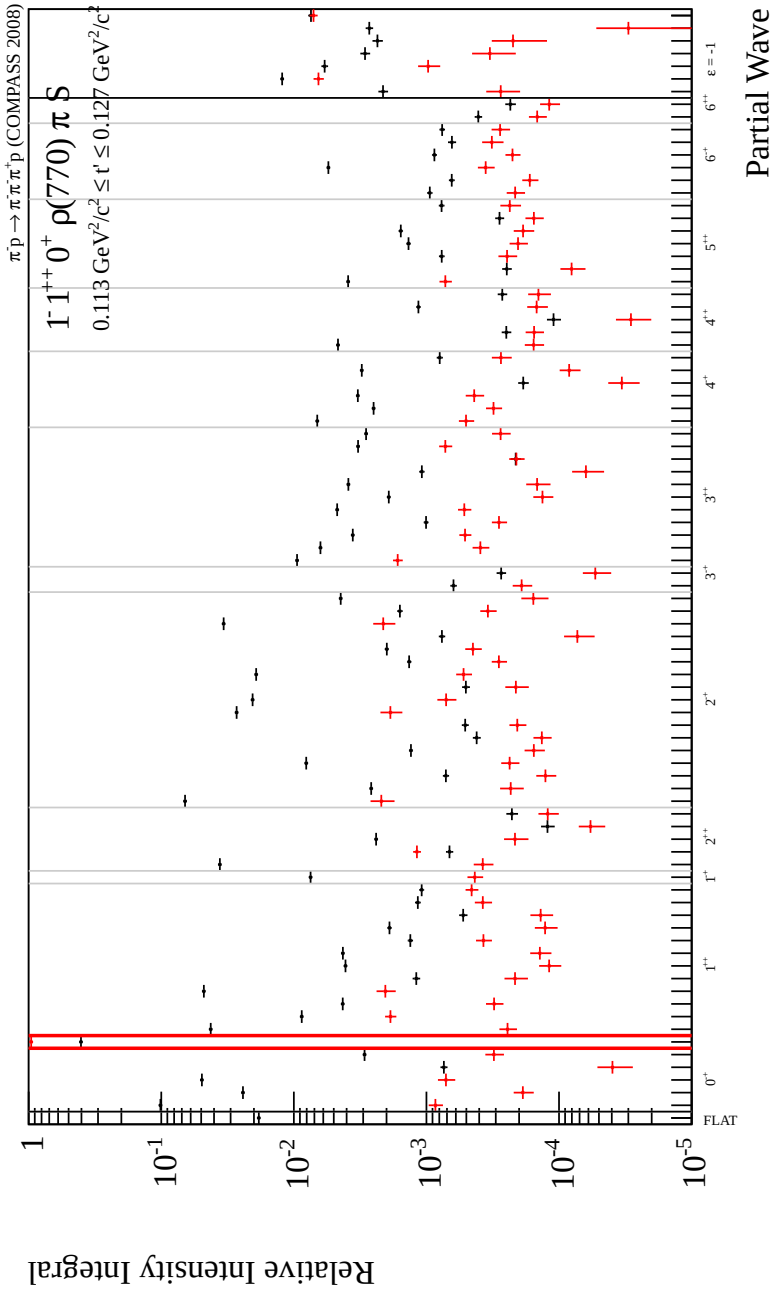

Figure 4.4: Overview of the relative Intensity Integral for each partial wave. In black the distribution containing all partial waves is shown. In red the distribution for events created for the $1^{++}\, 0^+\, \rho(770)\, \pi\, S$ wave (marked by the red lines) is shown.

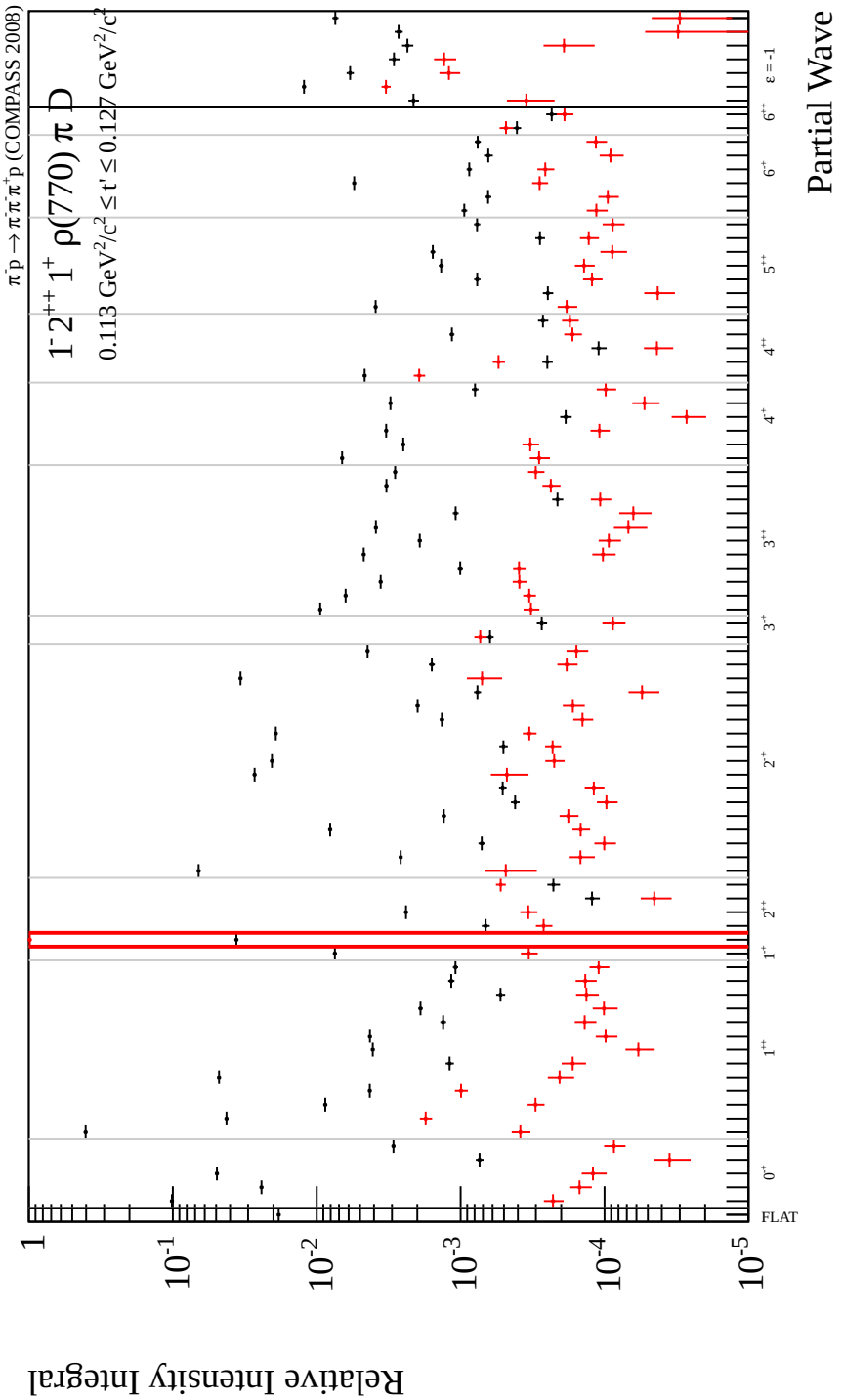

Figure 4.5: Overview of the relative Intensity Integral for each partial wave. In black the distribution containing all partial waves is shown. In red the distribution for events created for the $2^{++}\, 1^+\, \rho(770)\, \pi\, D$ wave (marked by the red lines) is shown17

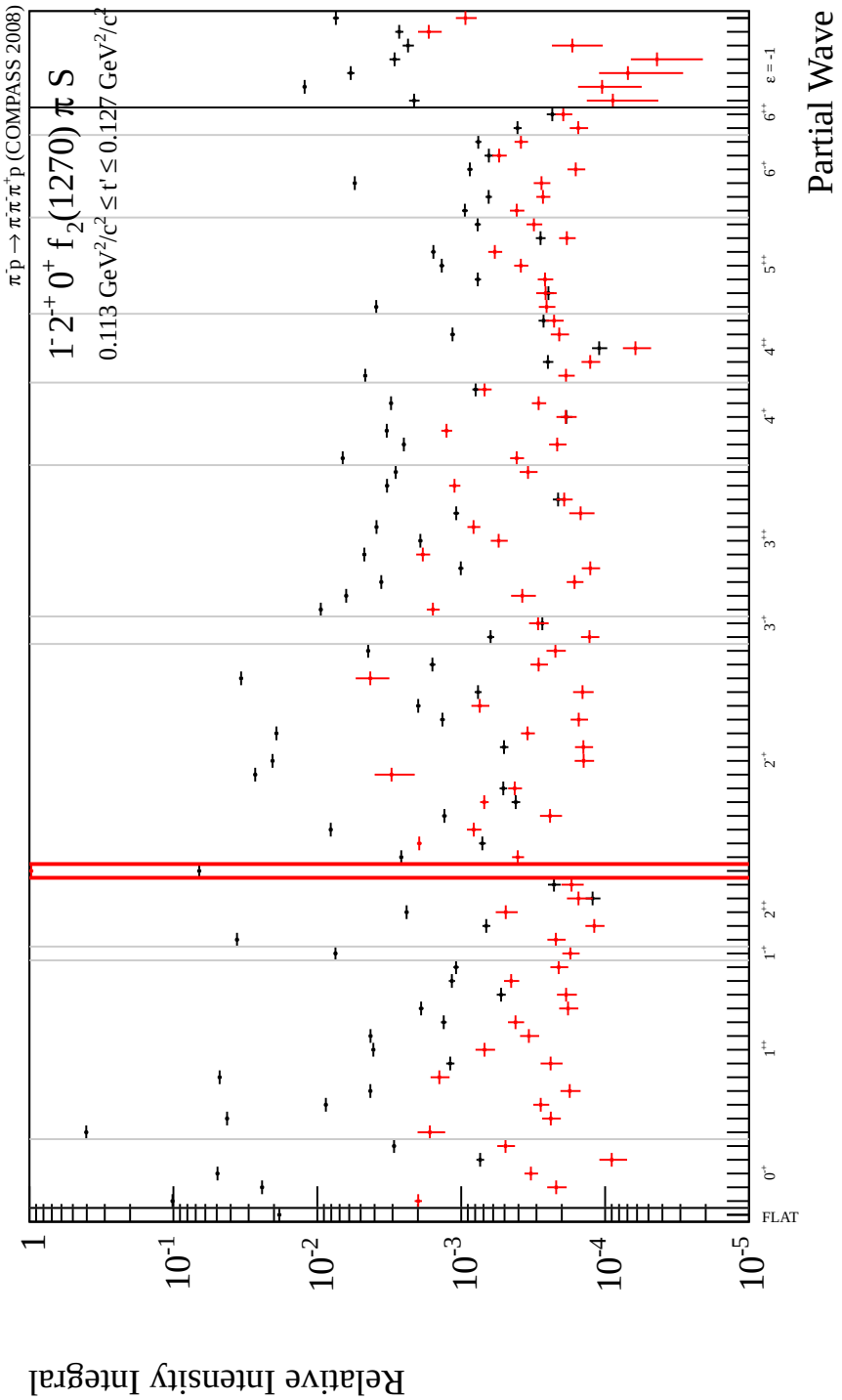

Figure 4.6: Overview of the relative Intensity Integral for each partial wave. In black the distribution containing all partial waves is shown. In red the distribution for events created for the $2^{-+}\,0^+\,f_2(1270)\,\pi\,S$ wave (marked by the red lines) is shown.

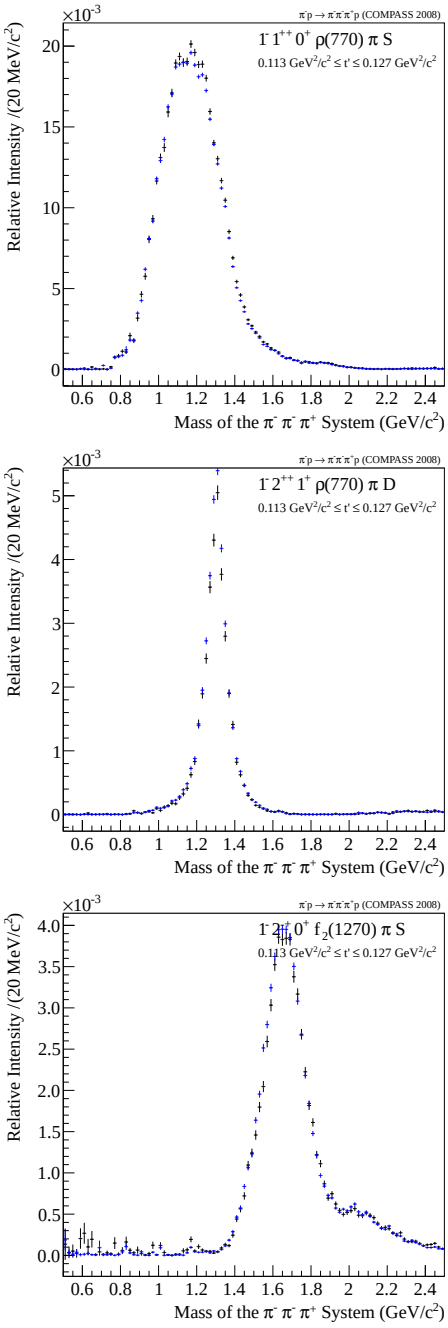

Figure 4.7: Plot of the three pion mass $m_{3\pi}$ for the three major waves. In black the distribution for the full set of partial waves is shown, in blue the corresponding real data intensities. The top row shows $1^{++}\,0^+\,\rho(770)\,\pi\,S$, the middle row $2^{++}\,1^+\,\rho(770)\,\pi\,D$and the bottom row shows $2^{-+}\,0^+\,f_2(1270)\,\pi\,S$.

4.3 Leakage into the two Waves of importance

The $1^{-+}\,1^{+}\,\rho(770)\,\pi\,P$partial wave is associated to a possible exotic hybrid state $J^{PC} = 1^{-+}$. The leakage study for this partial wave is very important, since it shows, that the observed intensity is not biased by leakage. As shown in figure 4.9 the intensity for this wave stays two orders of magnitude lower if it is not created but all other waves are created. The total leakage is about less than 4%. In figure 4.8 the distribution of the $m_{3\pi}$ is shown for both important partial waves.

Looking at $1^{++}\,0^{+}\,f_0(980)\,\pi\,P$the leakage is much higher. This can be because its intensity is lower than the one of $1^{-+}\,1^{+}\,\rho(770)\,\pi\,P$. For both waves there is leakage for masses above $2.2\,\mathrm{GeV}/c^2$ which is negligible because the only region of interest is around the peak and there the leakage stays very low.

Partial wave	t'–bin 2	t'–bin 9
$1^{-+}\,1^{+}\,\rho(770)\,\pi\,P$	0.0377	0.0216
$1^{++}\,0^{+}\,f_0(980)\,\pi\,P$	0.1002	0.0843

Table 4.3: Leakage into the special waves. The total intensity integral from the leakage run is compared to the reference run.

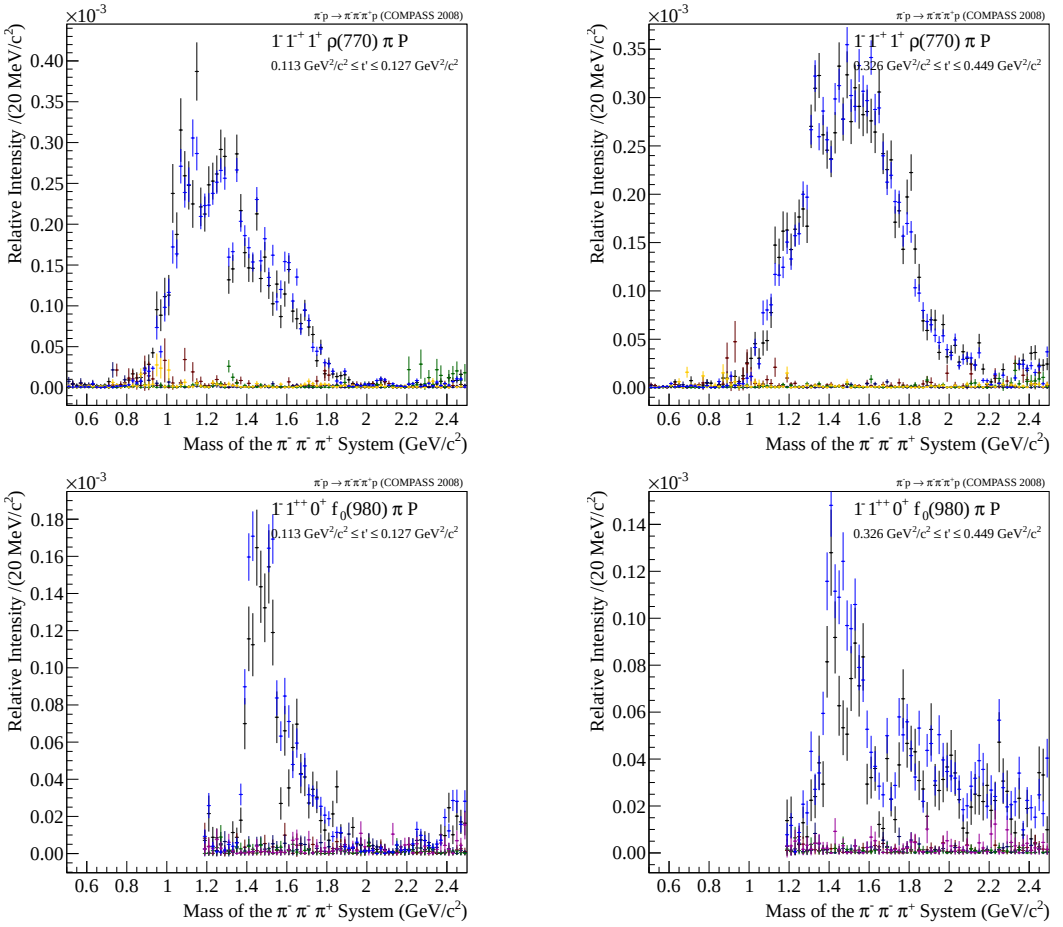

Figure 4.8: Plot of the three pion mass $m_{3\pi}$ for t'-bin 2(left) and t'-bin 9(right). In black the distribution for the full partial wave set is shown, in blue the real data intensity and in the other colors the four different leakage studies are shown. The top row shows $1^{-+}\,1^{+}\,\rho(770)\,\pi\,P$, the bottom $1^{++}\,0^{+}\,f_0(980)\,\pi\,P$.

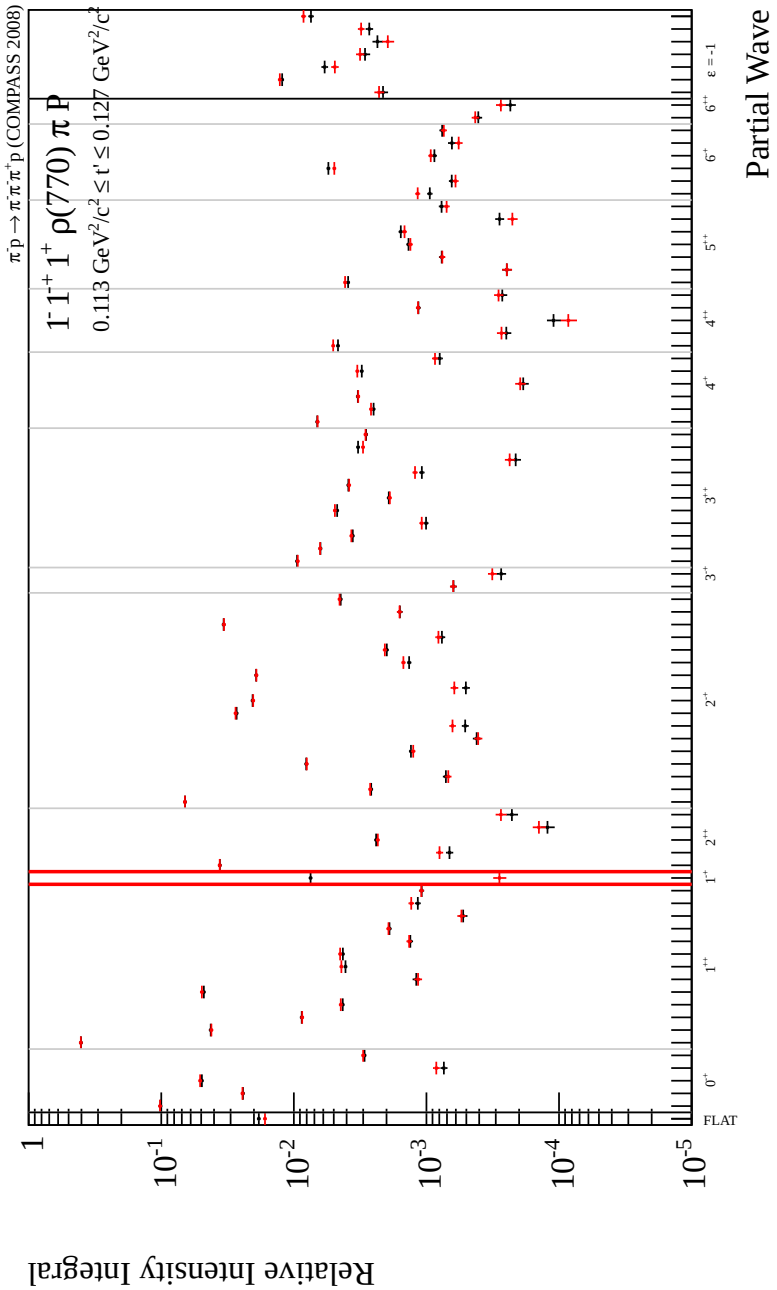

Figure 4.9: Overview of the leakage into the $1^{-+}\,1^+\,\rho(770)\,\pi\,P$. Shown is the total intensity integral for each wave relative to the total intensity integral of all waves. In red the sample without $1^{-+}\,1^+\,\rho(770)\,\pi\,P$and in black the reference with all partial waves is shown. $1^{-+}\,1^+\,\rho(770)\,\pi\,P$is marked by the red lines.

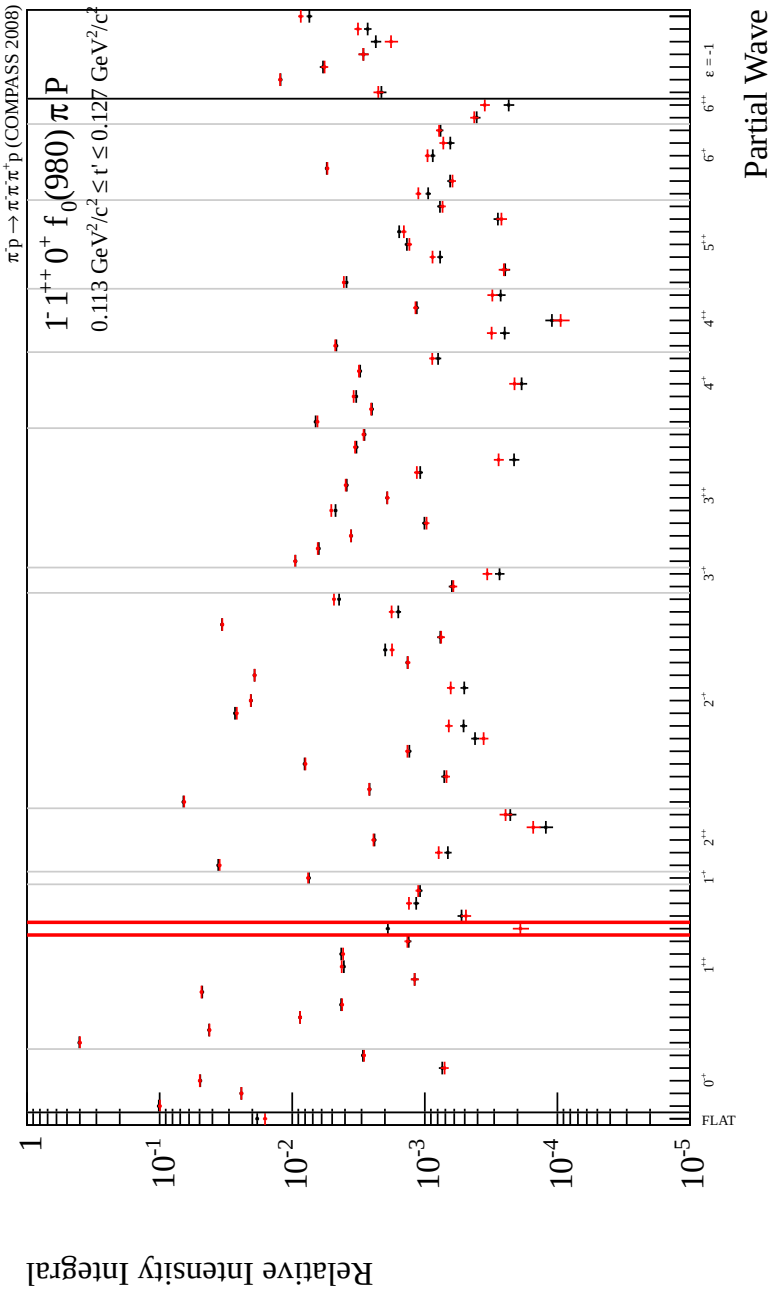

Figure 4.10: Overview of the leakage into the $1^{++}\,0^+\,f_0(980)\,\pi\,P$. Shown is the total intensity integral for each wave relative to the total intensity integral of all waves. In red the sample without $1^{++}\,0^+\,f_0(980)\,\pi\,P$and in black the reference with all partial waves is shown. $1^{++}\,0^+\,f_0(980)\,\pi\,P$is marked by the red lines.

5 Conclusion and Outlook

During this bachelor thesis 10 leakage studies were performed to analyze the leakage from the major waves and into the important waves. As a result the maximum leakage is around 10%. This leakage is negligible because it is not producing the observed peaks. The observed interesting distributions are not caused by leakage. The aim of this thesis was not to find the sources of leakage because that would take at least one year, but to find the order of magnitude leakage is present and to clarify that the peaks are no artifacts.

To accomplish this goal events were generated according to a specific distribution. These were simulated with a Monte Carlo chain. The last step was performing a partial wave analysis on this data.

A leakage study is a mandatory component of a systematic partial wave analysis. A future paper regarding one of the partial waves discussed in this thesis will include the leakage results obtained during this study.

For a complete study involving all 88 partial waves one would need to create a leakage matrix requiring at least 176 data samples per t'-bin. This would take about a year of simulation on the available computer cluster. Because this is far too much one could also look for leakage by adjusting the model and comparing the different fit results.

To completely remove leakage one would need detectors with a Plank scale resolution and no matter inside the spectrometer. For the analysis one would need computers with infinite computing power. Because this is fiction leakage will never be completely removed.

6 Acknowledgment

I would like to thank Professor Stephan Paul for giving me chance to participate in the analysis of the recent COMPASS data.

A special thank goes to Florian Haas for introducing me to all the needed programs and supporting me during this thesis.

Without the help of Boris Grube i would have spent countless hours reading into the theory of partial wave analysis. His easy to understand explanations made it a joy to learn new things.

I would like to thank all other members of the E18 for the great working atmosphere.

A Appendix

For the sake of completeness all overview plots for $t^{'}$–bin 9 are included in this chapter together with the full wave set and the table showing the $t^{'}$ ranges for each bin.

11 t′ bins [GeV$^2/c^2$]	Name
0.100000-0.112853	$t^{'}$–bin 1
0.112853-0.127471	$t^{'}$–bin 2
0.127471-0.144385	$t^{'}$–bin 3
0.144385-0.164401	$t^{'}$–bin 4
0.164401-0.188816	$t^{'}$–bin 5
0.188816-0.219907	$t^{'}$–bin 6
0.219907-0.262177	$t^{'}$–bin 7
0.262177-0.326380	$t^{'}$–bin 8
0.326380-0.448588	$t^{'}$–bin 9
0.448588-0.724294	$t^{'}$–bin 10
0.724294-1.000000	$t^{'}$–bin 11

Table A.1: Overview of the fragmentation of the t' spectrum used for this analysis.

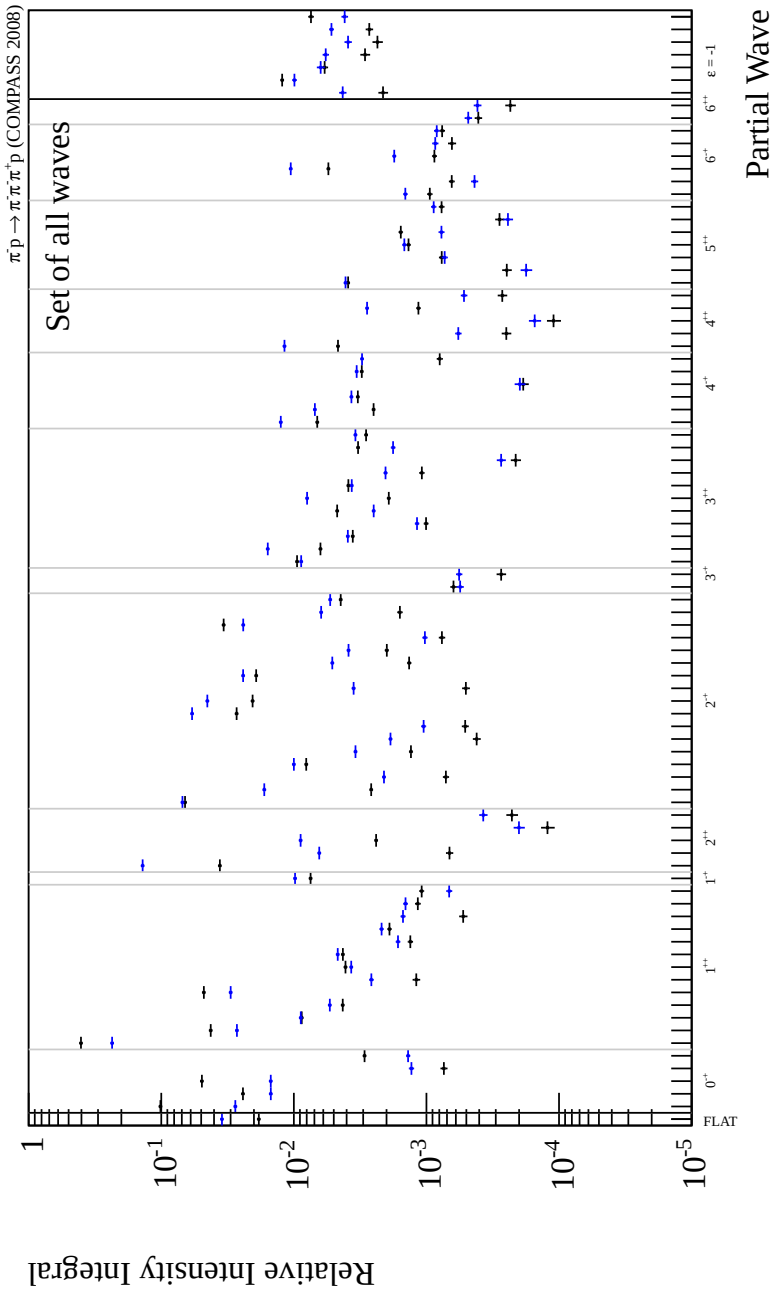

Figure A.1: Comparison of the two different t'–bins for the reference monte carlo data. In black t'–bin 2 is shown, t'–bin 9 is shown in blue. There are differences but these differences don't affect the output of a leakage study.

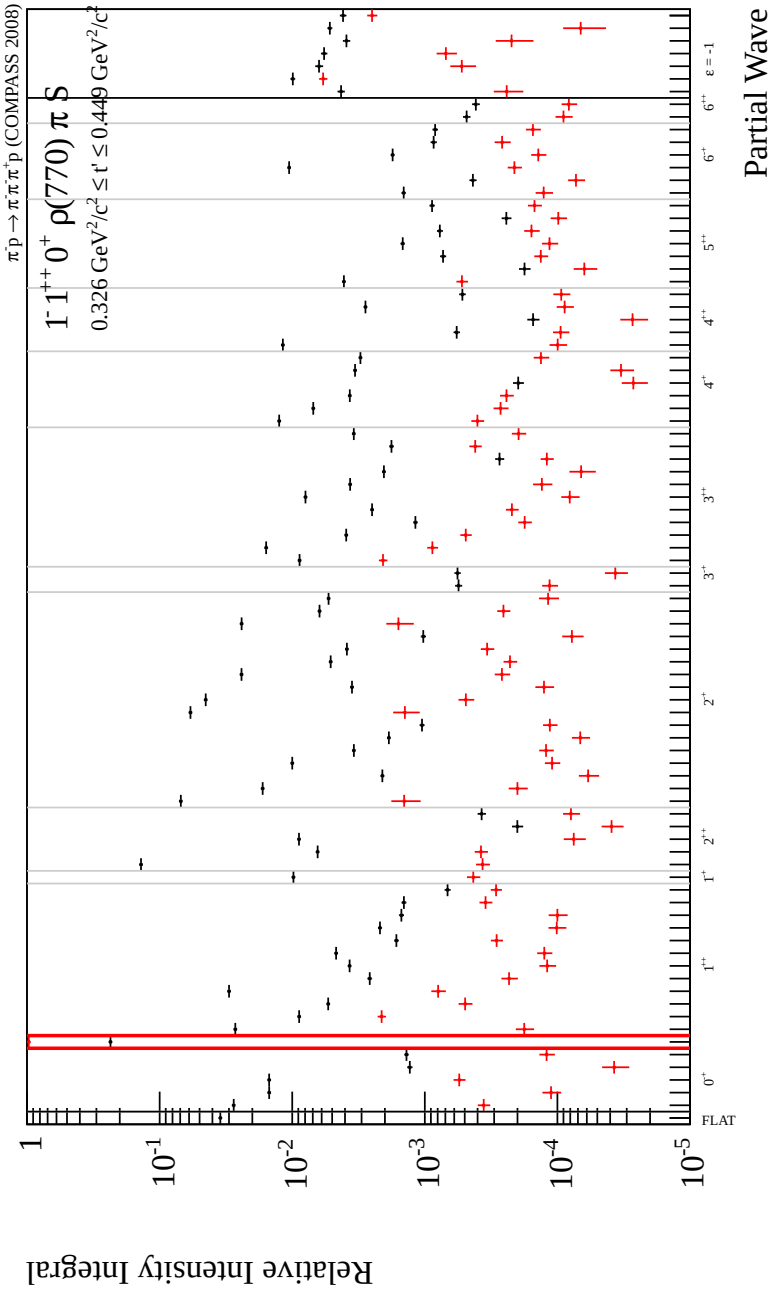

Figure A.2: Overview of the relative Intensity Integral for each partial wave. In black the distribution containing all partial waves is shown. In red the distribution for events created for the $1^{++}\, 0^+\, \rho(770)\, \pi\, S$ wave (marked by the red lines) is shown.

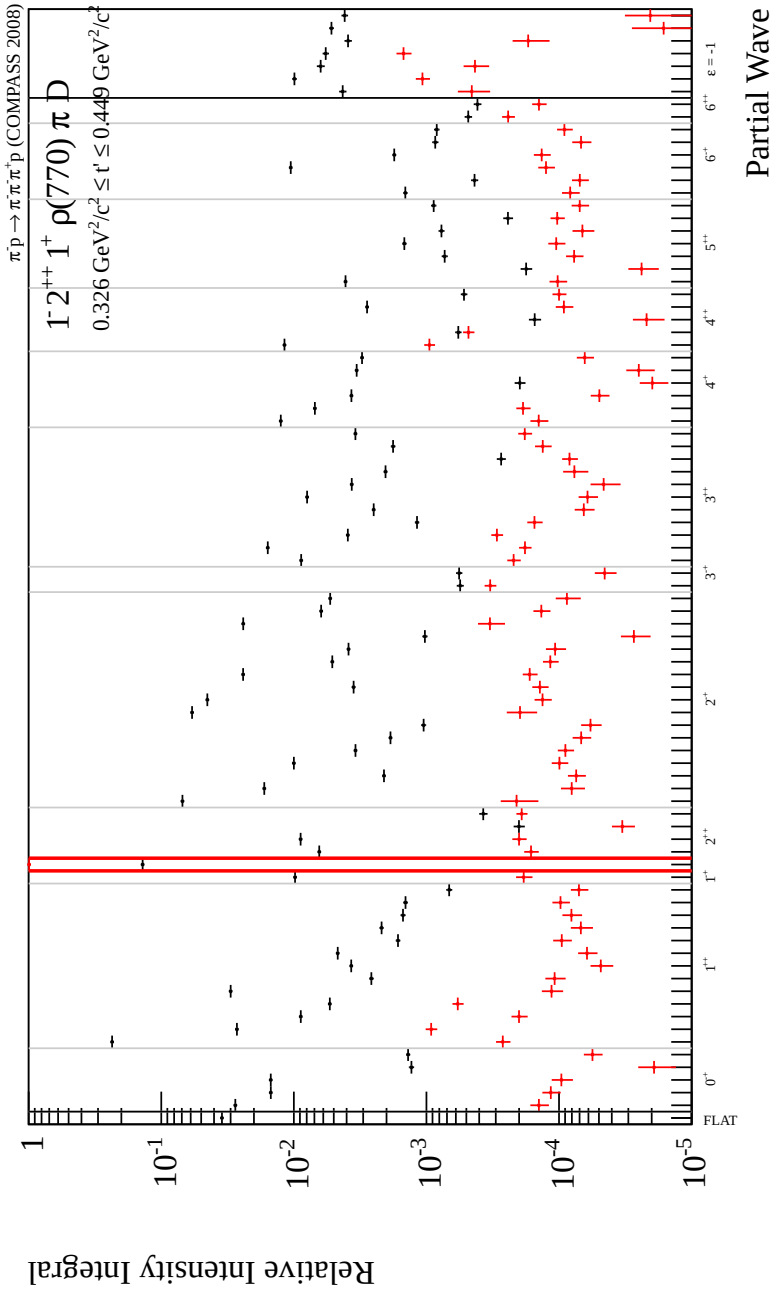

Figure A.3: Overview of the relative Intensity Integral for each partial wave. In black the distribution containing all partial waves is shown. In red the distribution for events created for the $2^{++}\ 1^+\ \rho(770)\,\pi\,D$ wave (marked by the red lines) is shown.

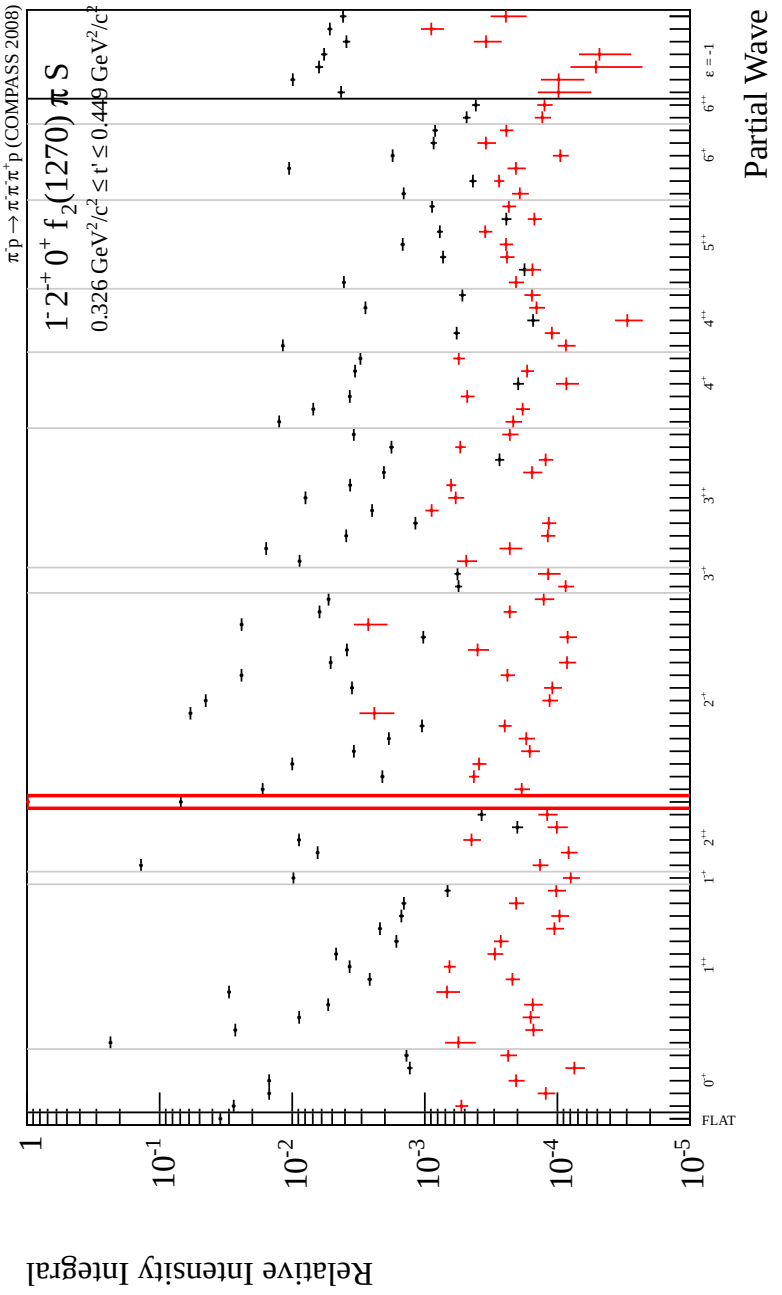

Figure A.4: Overview of the relative Intensity Integral for each partial wave. In black the distribution containing all partial waves is shown. In red the distribution for events created for the $2^{-+}\,0^+\,f_2(1270)\,\pi\,S$ wave (marked by the red lines) is shown.

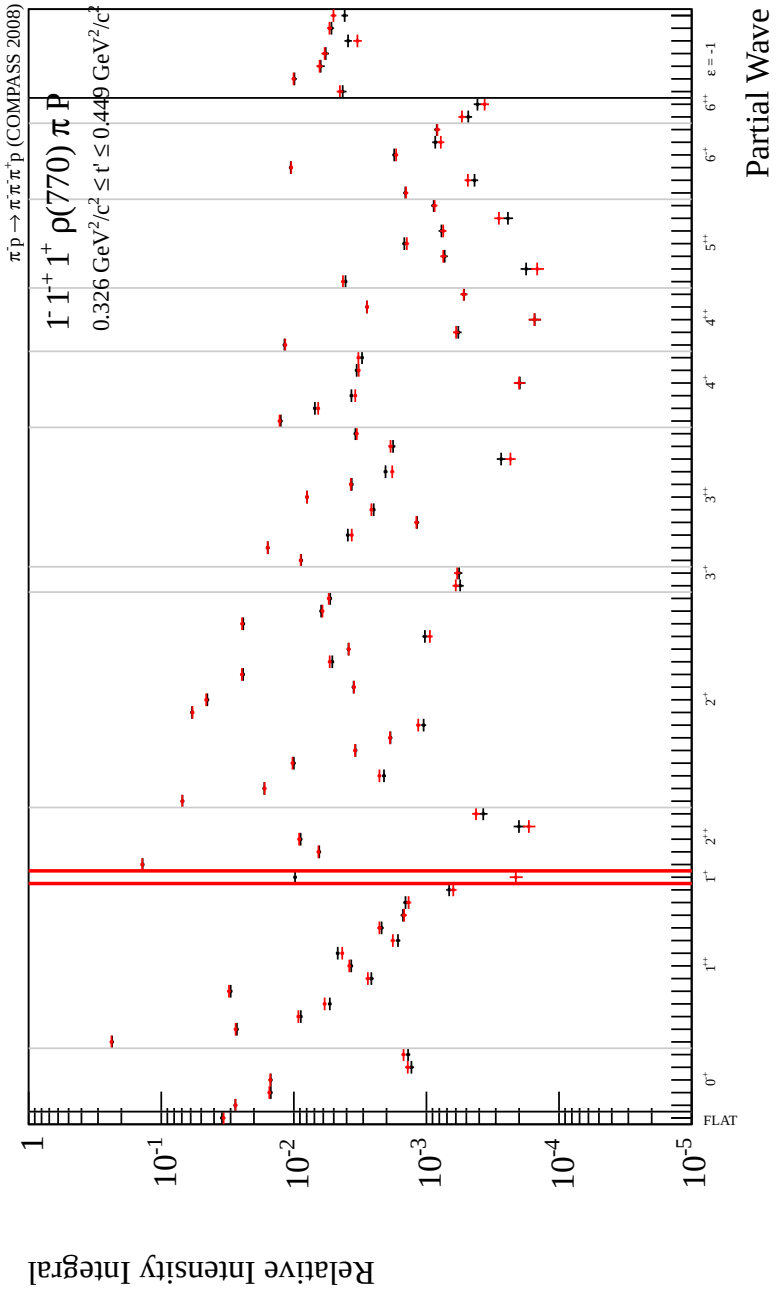

Figure A.5: Overview of the relative Intensity Integral for each partial wave. In black the distribution containing all partial waves is shown. In red the distribution for events created for the $1^{-+}\, 1^+\, \rho(770)\, \pi\, P$ wave (marked by the red lines) is shown.

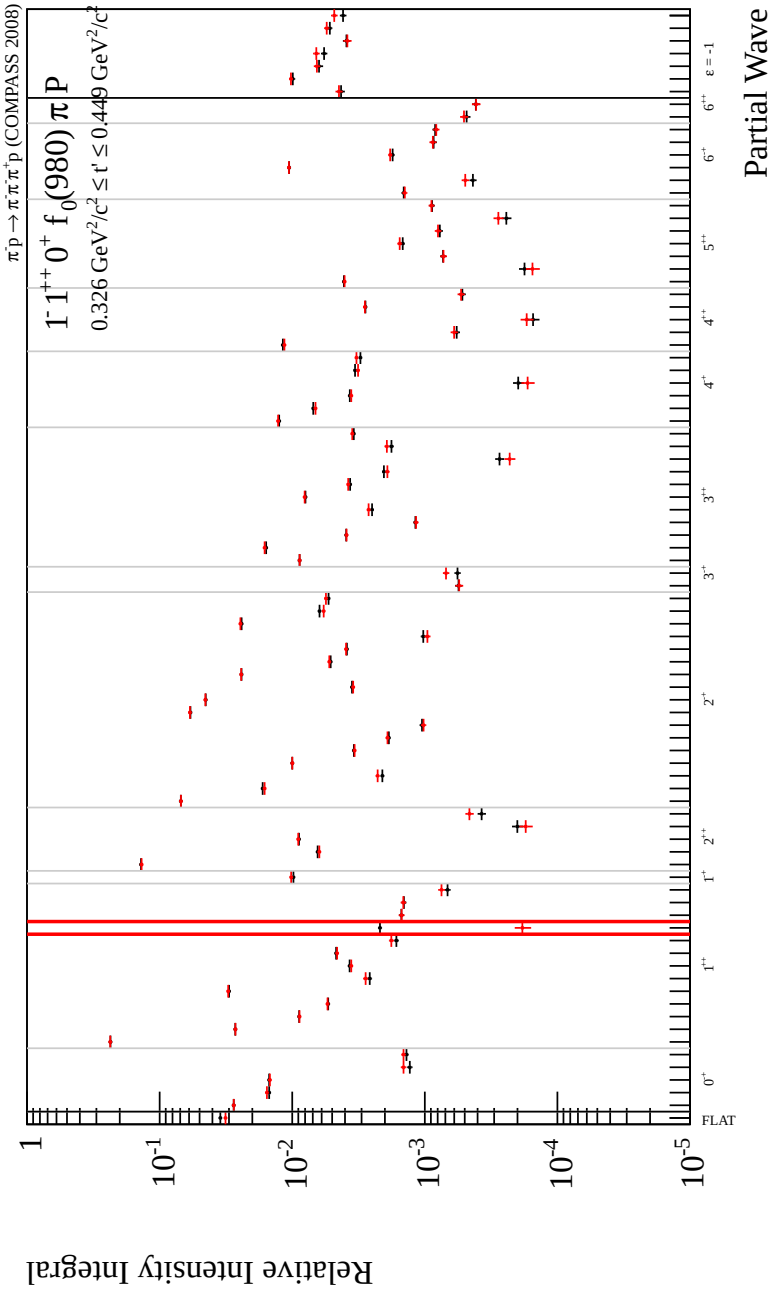

Figure A.6: Overview of the relative Intensity Integral for each partial wave. In black the distribution containing all partial waves is shown. In red the distribution for events created for the $1^{++}\,0^+\,f_0(980)\,\pi\,P$ wave (marked by the red lines) is shown.

$J^{PC}M^{\varepsilon}$	Isobar	L	Threshold
FLAT			-
$0^{-+}0^{+}$	$(\pi\pi)_S$	S	-
$0^{-+}0^{+}$	$f_0(980)$	S	1.20
$0^{-+}0^{+}$	$\varrho(770)$	P	-
$0^{-+}0^{+}$	$f_0(1500)$	S	1.70
$0^{-+}0^{+}$	$f_2(1270)$	S	-
$1^{++}0^{+}$	$\varrho(770)$	S	-
$1^{++}1^{+}$	$\varrho(770)$	S	-
$1^{++}0^{+}$	$\varrho(770)$	D	-
$1^{++}1^{+}$	$\varrho(770)$	D	-
$1^{++}0^{+}$	$(\pi\pi)_S$	P	-
$1^{++}1^{+}$	$(\pi\pi)_S$	P	1.1
$1^{++}0^{+}$	$f_2(1270)$	P	1.22
$1^{++}1^{+}$	$f_2(1270)$	P	-
$1^{++}0^{+}$	$f_2(1270)$	F	-
$1^{++}0^{+}$	$f_0(980)$	P	1.18
$1^{++}1^{+}$	$f_0(980)$	P	1.14
$1^{++}0^{+}$	$\varrho_3(1690)$	D	-
$1^{++}0^{+}$	$\varrho_3(1690)$	G	-
$1^{-+}1^{+}$	$\varrho(770)$	P	-
$2^{++}1^{+}$	$\varrho(770)$	D	-
$2^{++}2^{+}$	$\varrho(770)$	D	-
$2^{++}1^{+}$	$f_2(1270)$	P	1.00
$2^{++}2^{+}$	$f_2(1270)$	P	1.40
$2^{++}1^{+}$	$\varrho_3(1690)$	D	0.80
$2^{-+}0^{+}$	$f_2(1270)$	S	-
$2^{-+}1^{+}$	$f_2(1270)$	S	1.1
$2^{-+}2^{+}$	$f_2(1270)$	S	-
$2^{-+}0^{+}$	$f_2(1270)$	D	-
$2^{-+}1^{+}$	$f_2(1270)$	D	-
$2^{-+}2^{+}$	$f_2(1270)$	D	-
$2^{-+}0^{+}$	$f_2(1270)$	G	-
$2^{-+}0^{+}$	$\varrho(770)$	P	-
$2^{-+}1^{+}$	$\varrho(770)$	P	-
$2^{-+}2^{+}$	$\varrho(770)$	P	-
$2^{-+}0^{+}$	$\varrho(770)$	F	-
$2^{-+}1^{+}$	$\varrho(770)$	F	-
$2^{-+}0^{+}$	$\varrho_3(1690)$	F	1.00
$2^{-+}1^{+}$	$\varrho_3(1690)$	F	1.30
$2^{-+}0^{+}$	$(\pi\pi)_S$	D	-
$2^{-+}1^{+}$	$(\pi\pi)_S$	D	-
$2^{-+}0^{+}$	$f_0(980)$	D	1.16
$3^{-+}1^{+}$	$\varrho(770)$	F	-
$3^{-+}1^{+}$	$f_2(1270)$	D	1.34
$3^{++}0^{+}$	$\varrho(770)$	D	-
$3^{++}1^{+}$	$\varrho(770)$	D	-
$3^{++}0^{+}$	$\varrho(770)$	G	-
$3^{++}1^{+}$	$\varrho(770)$	G	-
$3^{++}0^{+}$	$f_2(1270)$	P	0.96
$3^{++}1^{+}$	$f_2(1270)$	P	1.14
$3^{++}0^{+}$	$\varrho_3(1690)$	S	1.38
$3^{++}1^{+}$	$\varrho_3(1690)$	S	1.38
$3^{++}0^{+}$	$\varrho_3(1690)$	6	-
$3^{++}0^{+}$	$(\pi\pi)_S$	F	1.38
$3^{++}1^{+}$	$(\pi\pi)_S$	F	1.38
$4^{-+}0^{+}$	$\varrho(770)$	F	-
$4^{-+}1^{+}$	$\varrho(770)$	F	-
$4^{-+}0^{+}$	$f_2(1270)$	D	-
$4^{-+}1^{+}$	$f_2(1270)$	D	-
$4^{-+}0^{+}$	$f_2(1270)$	G	1.6
$4^{-+}0^{+}$	$(\pi\pi)_S$	G	1.4
$4^{++}1^{+}$	$\varrho(770)$	G	-
$4^{++}2^{+}$	$\varrho(770)$	G	-
$4^{++}1^{+}$	$\varrho_3(1690)$	D	1.7
$4^{++}1^{+}$	$f_2(1270)$	F	-
$4^{++}2^{+}$	$f_2(1270)$	F	-
$5^{++}0^{+}$	$\varrho(770)$	G	-
$5^{++}0^{+}$	$\varrho_3(1690)$	D	1.36
$5^{++}0^{+}$	$f_2(1270)$	F	0.98
$5^{++}1^{+}$	$f_2(1270)$	F	-
$5^{++}0^{+}$	$f_2(1270)$	H	-
$5^{++}0^{+}$	$(\pi\pi)_S$	H	-
$5^{++}1^{+}$	$(\pi\pi)_S$	H	-
$6^{-+}0^{+}$	$(\pi\pi)_S$	6	-
$6^{-+}1^{+}$	$(\pi\pi)_S$	6	-
$6^{-+}0^{+}$	$\varrho(770)$	H	-
$6^{-+}1^{+}$	$\varrho(770)$	H	-
$6^{-+}0^{+}$	$\varrho_3(1690)$	F	-
$6^{-+}0^{+}$	$f_2(1270)$	G	-
$6^{++}1^{+}$	$\varrho(770)$	6	-
$6^{++}1^{+}$	$f_2(1270)$	H	-
$1^{++}1^{-}$	$\varrho(770)$	S	-
$1^{-+}0^{-}$	$\varrho(770)$	P	-
$1^{-+}1^{-}$	$\varrho(770)$	P	-
$2^{++}0^{-}$	$\varrho(770)$	D	-
$2^{++}0^{-}$	$f_2(1270)$	P	1.18
$2^{++}1^{-}$	$f_2(1270)$	P	1.3
$2^{-+}1^{-}$	$f_2(1270)$	S	-

Table A.2: Waveset used both for proton and lead data. 80 amplitudes with positive reflectivity, 7 with negative.

Bibliography

[1] COMPASS Collaboration. Observation of a $J^{PC} = 1^{-+}$ exotic resonance in diffractive dissociation of 190 GeV/c π^- into π^- π^- π^+. Technical report, COMPASS group, 2009.

[2] Sergei Gerassimov. Physics analysis software tools, 2011.

[3] The COMPASS group. The compass experiment at cern. Technical report, CERN, 2007.

[4] F. Haas. *Precision Meson Spectroscopy: Diffractive Dissociation of* $\pi^- + p \text{ -> } \pi^-$ π^- $\pi^+ + p$. PhD thesis, Technical University Munich, expected October 2013.